Climate Dynamics
https://doi.org/10.1007/s00382-020-05382-4

# The abyssal origins of North Atlantic decadal predictability

Stephen Yeager[1]

Received: 10 February 2020 / Accepted: 13 July 2020


**Abstract**
The fundamental mechanisms that explain high subpolar North Atlantic (SPNA) decadal predictability within a particular modeling framework are described. The focus is on the Community Earth System Model (CESM), run in both a historical forced-ocean configuration as well as in a fully coupled configuration initialized from the former. The initialized prediction experiments comprise the CESM Decadal Prediction Large Ensemble (CESM-DPLE)—a 40-member set of retrospective hindcasts documented in Yeager et al. (Bull Am Meteorol Soc 99:1867–1886. https://doi.org/10.1175/bams-d-17-0098.1, 2018). Heat budget analysis confirms the driving role of advective heat convergence in skillful prediction of SPNA upper ocean heat content out to decadal lead times. The key ocean dynamics are topographically-coupled overturning/gyre fluctuations that are geographically centered over the mid-Atlantic ridge (MAR). Long-lasting predictive skill for ocean heat transport can be related to predictable barotropic gyre and sigma-coordinate AMOC circulations, but depth-coordinate AMOC is far less predictable except in the deepest layers. The foundation of ocean memory (and circulation predictive skill) in CESM-DPLE is Labrador Sea Water thickness, which propagates predictably through interior pathways towards the MAR where large anomalies accumulate and persist. Abyssal thickness anomalies drive predictable decadal changes in the gyre circulation, including changes in sea level gradient and near surface flow, that account for the high predictability of SPNA upper ocean heat content.

**Keywords** Decadal prediction · North Atlantic · Subpolar gyre · AMOC

## 1 Introduction

Recent studies offer compelling evidence that the subpolar North Atlantic Ocean is a region characterized by exceptionally high decadal predictability through the combined influence of external forcings and predictable internal variability related to large-scale ocean dynamics (Yeager and Robson 2017). Analyses of decadal hindcasts submitted to the 5th Coupled Model Intercomparison Project (CMIP5) consistently show that initialization (from observation-based state estimates) results in the largest positive impact on surface temperature skill in this region (e.g., Müller et al. 2012; Kirtman et al. 2013; Doblas-Reyes et al. 2013; Smith et al. 2019). The multidecadal variability of the Atlantic Meridional Overturning Circulation (AMOC) is commonly invoked as a key source of decadal ocean memory contributing to long-lasting prediction skill in the subpolar North Atlantic (SPNA), both for perfect model potential predictability (e.g., Griffies and Bryan 1997; Collins et al. 2006) as well as for real-world predictions (e.g., Robson et al. 2012; Yeager et al. 2012; Pohlmann et al. 2013; Msadek et al. 2014). However, the precise origins of decadal SPNA skill still remain rather obscure, due to gaps in our understanding of AMOC and SPNA variability mechanisms, uncertainty about the fidelity of model representation of key processes, and a lack of observations for ground truthing. In this study, we examine the predictability mechanisms at work in one state-of-the-art decadal prediction system—the Community Earth System Model Decadal Prediction Large Ensemble (CESM-DPLE; Yeager et al. 2018)—and find that high SPNA skill is primarily attributable to predictable subpolar gyre dynamics that link highly predictable deep water mass anomalies to near-surface volume and heat transport variations through the sea surface height field.

**Electronic supplementary material** The online version of this article (https://doi.org/10.1007/s00382-020-05382-4) contains supplementary material, which is available to authorized users.

✉ Stephen Yeager
yeager@ucar.edu

[1] National Center for Atmospheric Research, Boulder, CO, USA

Published online: 24 July 2020

The present exploration of SPNA predictability dynamics in CESM-DPLE builds on several previously published works that have shed light on historical Atlantic Ocean mechanisms at work in reanalysis-forced ocean–sea-ice (FOSI; see Sect. 2.1) simulations performed with the CESM ocean and sea-ice model components. Some salient prior results are summarized here to provide context for the analysis that will follow. The CESM FOSI AMOC exhibits a realistic mean strength at 26.5°N, although the Atlantic meridional heat transport appears to be slightly weaker than available estimates (Danabasoglu et al. 2014). The AMOC variability is dominated by a basin-scale, multidecadal fluctuation from anomalously weak overturning in the 1960s and 1970s, to peak overturning in the mid-1990s, and subsequent weakening towards climatological values (Danabasoglu et al. 2016). Yeager and Danabasoglu (2014) showed that this multidecadal AMOC variability can be ascribed to high-latitude buoyancy forcing, and specifically, to Labrador Sea density anomalies driven by winter surface flux anomalies associated with the North Atlantic Oscillation (NAO). The decomposition of FOSI interannual variability into buoyancy- and momentum-driven components in that study further revealed the dominant role of surface buoyancy forcing in generating variance in fields such as barotropic streamfunction (BSF), sea surface height (SSH), and near-surface flow, with the buoyancy-driven variance especially prominent north of about 35°N.

A dynamical explanation for the strong covariability between the overturning and subpolar gyre circulations in CESM FOSI was provided in Yeager (2015). That study established the dominance of bottom pressure torque (as opposed to wind stress curl) in the mean and time-varying vorticity balance of depth-integrated flow in the SPNA. It showed that the large-amplitude, buoyancy-driven, decadal AMOC fluctuations in FOSI are associated with deep flow anomalies that, through interaction with large bathymetric gradients along the western continental shelf and in the vicinity of the mid-Atlantic ridge (MAR), also drive large, decadal variations in the strength of the cyclonic subpolar gyre circulation. A composite difference between years of anomalously strong/weak high-latitude AMOC revealed strongly enhanced/weakened barotropic flow above the MAR between 40°N and 50°N (Fig. 10 of Yeager 2015), along with a much stronger/weaker Northern Recirculation Gyre (NRG) in line with Zhang and Vallis (2007).

Based on the aforementioned findings, Yeager et al. (2015) offered a sketch of the SPNA dynamics at work in a 10-member ensemble set of CESM1.0 initialized decadal hindcasts (submitted to CMIP5) that exhibited high skill at predicting decadal trends in Arctic winter sea ice extent. They argued that: (1) Labrador Sea density anomalies in FOSI in the upper 1000 m (and anticorrelated SSH anomalies) are forced by NAO variations and appear realistic; (2) the large decadal variations in water mass properties within the Labrador Sea region are not skillfully predicted on multi-year timescales; (3) the equatorward propagation of water mass (and associated SSH) signals from the Labrador Sea to the region east of the Grand Banks of Newfoundland, however, is highly predictable on multi-year timescales; (4) predictable SSH east of Grand Banks is linked to predictable gyre circulation and heat transport across 50°N; and (5) highly predictable ocean heat transport at the southern boundary of the subpolar gyre contributes significantly to initialization-enhanced SST skill in the SPNA.

A deeper understanding of the origins of decadal prediction skill is critical for advancing the field scientifically as well as for bolstering confidence in the use of decadal prediction data products by various stakeholders. This study elaborates on the ideas proposed in Yeager et al. (2015) in order to clarify how (ocean) initial condition information propagates through space and time to produce large skill enhancement in the SPNA region on decadal timescales. Several new findings suggest that the conventional emphasis on geostrophic AMOC (measured by boundary density fluctuations in depth coordinates) as the fundamental reservoir of decadal ocean memory contributing to initialization-enhanced decadal prediction skill should be reconsidered. In CESM-DPLE, the essential ocean memory resides in long-lasting abyssal LSW thickness anomalies that move slowly through interior pathways towards the western flank of the MAR where they induce highly predictable, decadal SSH (and surface geostrophic flow) anomalies. The relevant ocean dynamics are therefore primarily barotropic and relate to buoyancy-driven fluctuations in gyre strength that project strongly onto overturning in density space, but not onto overturning in depth space. The focus on a hindcast set from a single model (CESM-DPLE) allows for an in-depth examination of processes, but a drawback is that the conclusions will not necessarily hold in general for all decadal prediction systems.

## 2 Materials and methods

### 2.1 The prediction system

The CESM-DPLE is a set of 40-member hindcasts initialized each November 1 between 1954 and 2017 and integrated for 122 months, allowing for skill assessment through 10 full lead years. Yeager et al. (2018) provides a general overview of this community data resource, including details of the models used (CESM version 1.1), a description of the experimental design, and global skill assessments for fields such as upper ocean heat content, surface temperature, and precipitation. A key strength of CESM-DPLE is that it represents the initialized counterpart to the 40-member CESM

Large Ensemble (CESM-LE) set of historical simulations (1920–2100) that is documented in Kay et al. (2015). Joint analysis of CESM-DPLE and CESM-LE therefore permits robust discrimination between skill attributable to initialization versus that arising from external forcing, within a single-model framework. The dataset is freely available and has been submitted as NCAR's contribution to the Decadal Climate Prediction Project (DCPP) component of CMIP6, but it should be noted that both CESM-DPLE and CESM-LE use external forcings from CMIP5 (Kay et al. 2015). The preliminary analysis in Yeager et al. (2018) reveals that CESM-DPLE exhibits very high skill at predicting pentadal mean upper ocean heat content (UOHC; depth-averaged temperature between 0 and 295 m) and sea surface temperature (SST) in the SPNA out to decadal lead times. In line with many other studies (some cited above), the SPNA stands out as a region of particularly high skill enhancement associated with initialization.

The ocean and sea-ice initial conditions used for CESM-DPLE come from a forced ocean—sea-ice (FOSI) simulation designed to imprint relatively well-sampled historical atmospheric information into the ocean and sea-ice without the use of data assimilation. FOSI simulations are reconstructions of historical ocean and sea-ice states obtained by forcing those model components with reanalysis-based atmospheric state and surface flux fields. The lack of direct constraint to observed ocean and sea-ice data in such runs may result in less-than-optimal state reconstructions, particularly over recent years characterized by a dramatic increase in ocean/sea-ice observations via profiling floats and satellites, but there are also potential advantages to the FOSI initialization approach for decadal prediction. FOSI runs are cheap and easy to perform, evaluate, and refine; they can be extended as far back in time as atmospheric observations/reanalyses permit; and they are fully prognostic solutions of the governing equations that admit detailed study of physical mechanisms (as done herein). Furthermore, it has been shown that ocean data assimiliation does not necessarily deliver more consistent reconstructions of key phenomena relevant to decadal prediction, such as multidecadal AMOC variability, than the much simpler FOSI method (Karspeck et al. 2015).

The ocean and sea-ice state reconstructions from such FOSI runs have been scrutinized in several recent multi-model studies (e.g., Griffies et al. 2014; Downes et al. 2015; Farneti et al. 2015; Wang et al. 2016a, b; Ilicak et al. 2016; Tseng et al. 2016). In the North Atlantic, many models (including CESM) produce encouragingly realistic mean and variability compared to available observations when run in FOSI mode (Danabasoglu et al. 2014, 2016), but potentially non-trivial biases are also found that are likely related to both the coarse (nominal 1° in the horizontal) model resolution as well as errors in the atmospheric forcing fields. Known biases include: low ocean kinetic energy, poorly represented Gulf Stream (GS) and North Atlantic Current (NAC) pathways, unresolved overflow physics, and excessive deep water production (Li et al. 2019). The high skill of CESM-DPLE in the North Atlantic suggests that such errors in the CESM FOSI are not fatal flaws, but mechanisms diagnosed from such simulations should be treated with caution.

CESM-DPLE employs full field initialization with historical ocean and sea-ice states obtained from a FOSI simulation that uses the same model version (CESM1.1), but with ocean and sea-ice as the only active model components. The FOSI run was initialized from observed temperature and salinity and spun up through 5 consecutive cycles of adjusted CORE (Coordinated Ocean-Ice Reference Experiment; Large and Yeager 2004, 2009; Griffies et al. 2009) forcing spanning 1948–2009. The salinity field in the FOSI run is constrained by nudging to surface climatology with a 4-year restoring timescale (see Appendix C of Danabasoglu et al. 2014). The ocean and sea-ice states from the fifth cycle (which was extended through 2017) were used as initial conditions. Refer to Yeager et al. (2018) for further details, including a discussion of modifications made to the standard CORE wind field. Initial conditions for the atmosphere and land model components of CESM-DPLE are selected from corresponding years of a single member of CESM-LE (#34), and hence only reflect the historical state through the influence of external forcings. The 40-member ensemble is generated through round-off perturbations to the atmospheric temperature field.

## 2.2 Skill evaluation and statistical significance

Spurious climate drifts associated with full field initialization are removed prior to skill evaluation using the mean drift correction technique (Choudhury et al. 2017), but de-drifted fields are analyzed as anomalies and so model fields are not re-referenced to observed climatology in the drift correction step (for details, see: Yeager et al. 2018). In the absence of observations for many fields of interest, CESM-DPLE hindcast evolution will be assessed relative to FOSI—the version of historical ocean truth presented to the coupled model through initialization. The potential predictability of CESM-DPLE is thus evaluated in terms of anomaly correlations (Pearson's r) between the 40-member ensemble mean and the FOSI simulation for assorted fields.

Except where otherwise noted, statistical significance is assessed using a non-parametric, block bootstrap technique (e.g., Goddard et al. 2013; Yeager et al. 2018; Smith et al. 2019). Specifically, p-values are computed by resampling the hindcasts (1000 times with replacement) across ensemble members and validation times (using a temporal block size of 5 years to account for autocorrelation in the time series) to build a probability distribution of skill scores. A Fisher's z-transform is applied to correlation scores prior to the determination of p-values. Statistically significant results are reported for p-values ≤ 0.05.

## 2.3 Model diagnostics

### 2.3.1 Predictable variance fraction

The large ensemble size used in CESM-DPLE (and CESM-LE) permits a more accurate estimation of the model's potentially predictable variance fraction (PVF) than is usually the case in decadal prediction studies. The PVF is quantified as in other studies (e.g., Boer et al. 2013; Eade et al. 2014; Scaife and Smith 2018) as:

$$PVF = \sigma^2_{sig} / \sigma^2_{tot} \tag{1}$$

where $\sigma^2_{sig}$ is the signal variance computed from the ensemble mean, and $\sigma^2_{tot}$ is the total variance computed as the expected value of the variance from individual members. Comparing PVF to the squared correlation ($r^2$) obtained from verifying against observations (or an observation-based reconstruction such as FOSI) highlights mismatches between the potential predictability quantified from ensemble spread and the prediction skill quantified from correlation. The ratio of predictable components (RPC; Eade et al. 2014; Scaife and Smith 2018; Smith et al. 2019) quantifies this mismatch as:

$$RPC = r / \sqrt{PVF} \tag{2}$$

where $r$ is a correlation value. This paper will draw attention to fields and regions where RPC<1, indicating that CESM-DPLE skill is lower than would be expected from the 40-member ensemble spread.

### 2.3.2 Upper ocean heat budget

We will consider fixed-depth upper ocean heat budgets from the CESM ocean component. All necessary terms have been saved to close the temperature tendency equation:

$$\begin{aligned}\int_D^{\eta} (\partial_t \theta) dz = &- \int_D^{\eta} \nabla \cdot (\mathbf{u}\theta + \mathbf{u}^* \theta) dz \\ &- \int_D^{\eta} (\nabla \cdot \mathbf{K}) dz + Q_{net} / (\rho_o C_p)\end{aligned} \tag{3}$$

where $D$ is a fixed depth level ($D = 295$ m is used throughout), $\eta$ is sea surface height; $\theta$ is temperature; $\mathbf{u}$ is the three-dimensional resolved velocity; $\mathbf{u}^*$ is the three-dimensional subgridscale velocity (which includes both mesoscale (Gent and Mcwilliams 1990) and submesoscale (Fox-Kemper et al. 2011) components); $\mathbf{K}$ is the three-dimensional diffusive flux; $Q_{net}$ is the net air-sea heat flux; $\rho_o$ is the ocean reference density; and $C_p$ is ocean heat capacity. The effects of subgridscale advection are bundled with the diffusive fluxes, so that the heat budget is decomposed in practice as follows:

$$\begin{aligned}\frac{1}{H}\left[\int_D^{\eta} (\partial_t \theta) dz\right] = &\frac{1}{H}\left[- \int_D^{\eta} \nabla \cdot (\mathbf{u}\theta) dz\right. \\ &\left. - \int_D^{\eta} \nabla \cdot (\mathbf{K} + \mathbf{u}^* \theta) dz + Q_{net} / (\rho_o C_p)\right]\end{aligned} \tag{4}$$

where $H = |D| + \eta$. The terms in Eq. 4 are accumulated at each model timestep (hourly) and archived as monthly means. They are referred to as (from left to right): TEND, ADV, MIX, and SHF (in units of °C/year).

### 2.3.3 Labrador sea water thickness

Model Labrador Sea Water (LSW) is defined using surface water mass formation analysis (e.g., Large and Nurser 2001; Langehaug et al. 2012) performed on monthly mean output of FOSI. The subpolar North Atlantic is divided into several subdomains in which monthly surface density flux is integrated over isopycnal outcrop areas (see Fig. ES1 in Online Resource 1). This analysis shows that there is a climatological annual surface production of model LSW in the density range $36.95 \leq \sigma_2 \leq 37.2$ kg m$^{-3}$. The strong NAO forcing of the late 1980s and early 1990s resulted in a pronounced shift towards denser-than-normal LSW in FOSI (Fig. ES1), as seen in hydrographic measurements (Yashayaev 2007). Given the prominent role of the early 1990s LSW signal in SPNA decadal predictability, we focus on this densest class of model LSW. LSW thickness ($\Delta z_{LSW}$) is therefore defined for both FOSI and CESM-DPLE as the thickness of the layer $37.025 \leq \sigma_2 \leq 37.175$ kg m$^{-3}$. The mean upper/lower depths of this layer in FOSI are roughly 1200 m/3400 m and the interannual standard deviation of the layer thickness exceeds 600 m in the Labrador Sea (see Fig. ES2 in Online Resource 1).

### 2.3.4 Geostrophic upper ocean velocity

Near surface meridional geostrophic flow is computed from observed and simulated sea surface height ($\eta$) as follows:

$$v = \frac{g}{f}\frac{\partial \eta}{\partial x} \tag{5}$$

where $g$ is gravitational acceleration (980.6 cm/s$^2$) and $f$ is the Coriolis parameter.

## 2.4 Observations

The observational data considered here include: (1) a station-based NAO index (https://climatedataguide.ucar.edu/climate-data/hurrell-north-atlantic-oscillation-nao-index

-station-based); (2) upper ocean heat content from the UK Met Office EN4.2.1 gridded ocean temperature product (Good et al. 2013); and (3) gridded mean sea level anomaly from multi-satellite altimetry observations obtained from Copernicus Marine Environment Monitoring Service (CMEMS; http://marine.copernicus.edu).

## 3 Results

### 3.1 Subpolar North Atlantic upper ocean heat content

Numerous studies have linked observed, multidecadal variations in SPNA upper ocean heat content (UOHC) to the delayed ocean dynamical response to NAO forcing (for a review, see Yeager and Robson 2017). A steady increase in winter NAO forcing from the early 1960s to the mid 1990s was accompanied by a decrease in SPNA UOHC, and an abrupt shift to weak NAO in the period from 1996 to 2012 corresponds to an anomalously warm period of the SPNA (Fig. 1). The FOSI simulation faithfully reproduces much of the observed variability in UOHC in the region albeit with a standard deviation that is too high compared to the EN4 data (0.55 °C compared to 0.37 °C). The CESM-DPLE skillfully predicts the evolution of annual mean SPNA UOHC out to decadal lead times (Fig. 1), particularly when verified against FOSI. This potential predictability (i.e., the ability of DPLE to reproduce FOSI) is the primary focus here that will permit tentative mechanistic attribution.

The high SPNA skill is associated with accurate ensemble mean forecasts of anomalously cold conditions between 1965 and 1995, warm conditions between 1996 and 2015, and the abrupt mid-1990s transition between these regimes. Although CESM-DPLE exhibits a cooling trend between 2010 and 2020 at all lead times (Fig. 1), the observed abrupt transition to anomalously cold conditions in the SPNA after 2015 is not well predicted. This behavior is the topic of ongoing investigation and is believed to be related to a failure to predict the highly anomalous surface fluxes in the winters of 2013/2014 and 2014/2015 that contributed to the intensity of the 2015 cold anomaly in the SPNA (e.g., Josey et al. 2018; Yeager et al. 2016). Unsmoothed (annual mean) data reveal that SPNA UOHC has rebounded to only slightly negative conditions in the last couple of years (Fig. ES3 in Online Resource 1), which has substantially reduced, but not eliminated, the discrepancy between recent CESM-DPLE hindcasts and observations.

CESM-DPLE exhibits very little degradation in SPNA UOHC skill as lead time increases (Fig. 1). The correlation score for lead years 1–5 (LY1-5) is 0.87 when verified against FOSI (0.58 when verified against EN4). The score for LY5-9 is only slightly lower at 0.84 (0.53). The

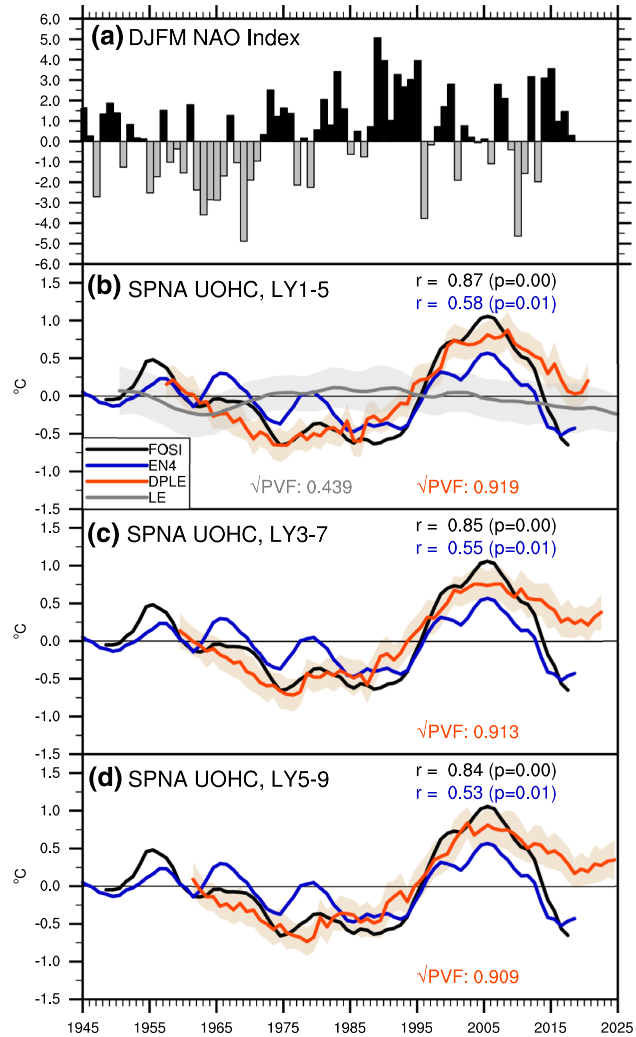


**Fig. 1** **a** Station-based winter (DJFM) NAO index. **b** Running 5-year mean SPNA upper ocean heat content (to 295 m depth) from EN4 observations (blue), FOSI (black), CESM-DPLE (red; average over lead years 1–5), and CESM-LE (grey). The SPNA region is defined as 45°W–20°W, 50°N–60°N (see black box in Fig. 3). The shading around CESM-DPLE and CESM-LE curves represents ensemble uncertainty ($\pm 1\sigma$). Correlations (and corresponding p-values) are given for CESM-DPLE verified against FOSI (black) and EN4 (blue). The square root of the predictable variance fraction ($\sqrt{PVF}$; see Sect. 2.3.1) is given for CESM-DPLE (red) and CESM-LE (grey), thus permitting direct comparison to correlation values. **c**, **d** Same as **b** but showing lead years 3–7 and 5–9, respectively

amplitude of the UOHC signal and the timing of the mid-1990s transition appears little changed between LY1-5 and LY5-9. Furthermore, the ensemble signal-to-noise characteristics (quantified in terms of predictable variance fraction or PVF; see Sect. 2.3.1) are also very stable. Direct comparison of $\sqrt{PVF}$ with FOSI correlation scores reveals that RPC < 1 for SPNA UOHC at all lead times, with the spread-based metric suggesting that more than 80% of variance in SPNA UOHC remains potentially predictable even out to LY5-9.

This can be compared to roughly 20% of predictable variance obtained in CESM-LE, whose ensemble average does not correlate significantly with either FOSI or EN4. The CESM-DPLE skill scores and PVF show similar stability with lead time if annual, rather than pentadal, means are considered (see Fig. ES3 in Online Resource 1). The fact that the phasing, amplitude, and spread of predicted SPNA UOHC varies so little with lead time (even out to LY10), and is so different from CESM-LE, strongly implies that the predictability must relate to a dynamical ocean mechanism and cannot be explained by damped persistence (see e.g., Yeager et al. 2018) and/or coupled model response to external forcings.

Examination of the upper ocean heat budget (see Sect. 2.3.2) from FOSI in the SPNA region sheds some preliminary light on the relevant mechanisms (Fig. 2). Both surface heat flux (SHF) and resolved advective heat convergence (ADV) are important terms in the multidecadal UOHC signal, and their anti-correlation supports the hypothesis of ocean-driven low-frequency variability in this region (Zhang et al. 2016; O'Reilly et al. 2016; Kim et al. 2020). Specifically, ADV (SHF) tendency anomalies are negative (positive) during the decades of SPNA cooling, and positive (negative) during the most recent warm decades. The net UOHC tendency is clearly the residual of large and covarying terms, and so it is difficult to determine causality from heat budget analysis alone. Nevertheless, since the variance of UOHC tendency is given by the sum of the variances and covariances of the terms included in the decomposition (ADV, SHF, and MIX; Eq. 4), some insight can be gained by comparing the relative magnitudes of these variances/covariances and how they change with timescale.

The spatial breakdown of UOHC budget variance is shown using raw (deseasonalized) monthly timeseries in Fig. 3, and using low-pass filtered timeseries (5 years and longer) in Fig. 4. Both figures show that ADV is the dominant term along the GS and its NAC extension into the central and eastern subpolar gyre. In panel h of both figures, we see strong negative covariance between ADV and MIX, particularly pronounced in regions where ADV variance is high and dominant, suggesting that diffusive mixing acts to damp anomalies generated by advective heat convergence in regions of strong surface flow. The covariance between ADV and SHF, however, exhibits an interesting difference after temporal smoothing. When all timescales are included, ADV and SHF show positive covariance over much of the subpolar domain (Fig. 3f), suggesting that high-frequency Ekman dynamics prevail (ie., stronger westerlies cool the upper ocean both through turbulent heat flux and by inducing anomalously southward Ekman flow). When multiyear and longer timescales are isolated, the covariance becomes almost uniformly negative over the domain, suggesting that high ADV variance along the NAC extension is damped by the SHF response (Fig. 4f) which adds to the larger damping effects of MIX (Fig. 4h). This interpretation is supported by the dominance of ADV variance along the GS path, the closely matching spatial patterns in the ADV covariance maps (Fig. 4f, h), and lead/lag analysis to be discussed below. Focusing on multiyear variance also changes the relative importance of terms when considering the SPNA region

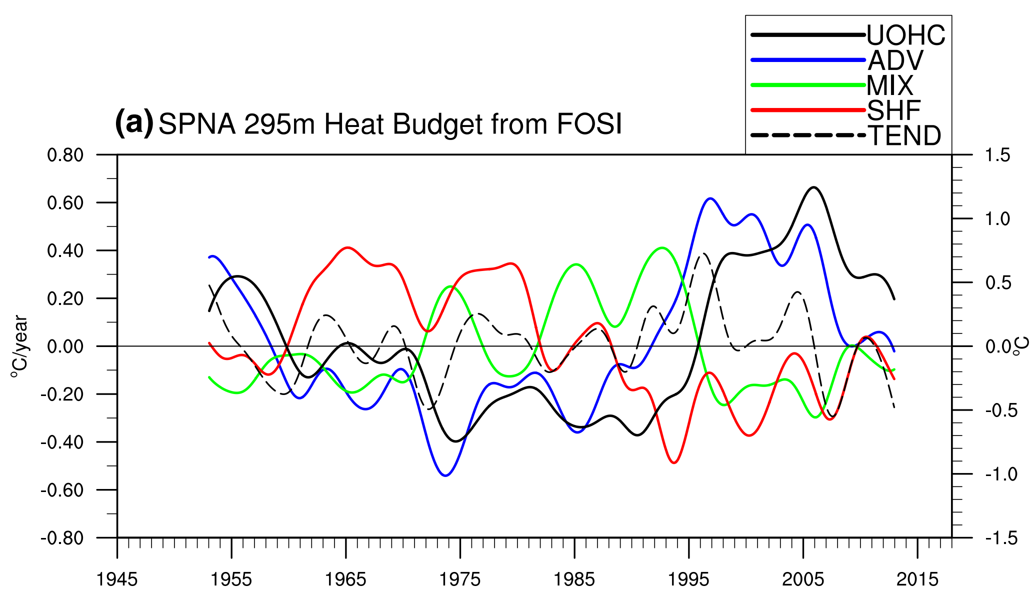


**Fig. 2** Upper ocean (to 295 m) heat content budget from FOSI for the SPNA region (45°W–20°W, 50°N–60°N; see black box in Fig. 3). The left axis is used for UOHC tendency terms, and the right axis is used for UOHC. All time series have been low-pass filtered with a Lanczos smoother with cutoff period of 60 months. Note that TEND is the sum of ADV, MIX, and SHF (see Sect. 2.3.2 for details)

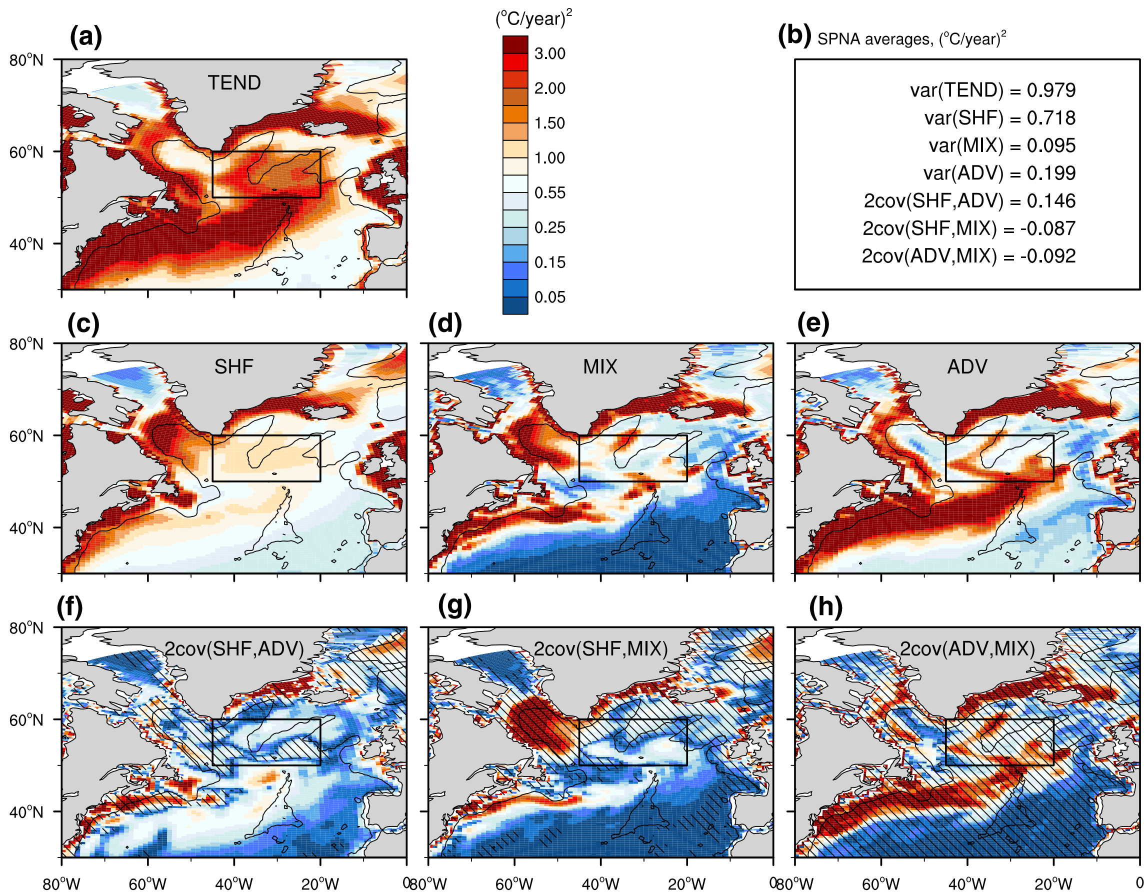


**Fig. 3** Upper ocean (to 295 m) FOSI heat budget variance (in units of (°C/year)$^2$) for: **a** TEND, **c** SHF, **d** MIX, **e** ADV, **f** 2cov (SHF, ADV), **g** 2cov (SHF, MIX), and **h** 2cov (ADV, MIX). Variance is computed from de-seasonalized monthly time series spanning 1948–2017. Cross-hatching indicates negative covariances. **b** Lists the variance decomposition after averaging terms over the SPNA region (black box; 45°W–20°, 50°N–60°N). Note nonlinear color scale and that the net tendency variance in (**a**) is equal to the sum of terms in (**c**–**h**). Thin black contour shows the 2500 m isobath

as a whole (compare Figs. 3b, 4b). Spatially-coherent SHF anomalies make this by far the dominant term when all timescales are included, even though locally within the SPNA SHF shows lower variance than ADV along strong current pathways. However, low-pass filtering dramatically reduces the role of SHF in the SPNA tendency budget, making ADV the primary driving term with lower-variance passive damping provided by SHF and MIX. The relative dominance of ADV in the SPNA heat budget on multiyear timescales underscores the relevance of this budget term for decadal prediction. These FOSI results largely corroborate recent examinations of North Atlantic mechanisms as represented in more formal ocean state estimation products (Buckley et al. 2014, 2015).

The high and long-lasting skill of CESM-DPLE is itself a compelling line of evidence for the causal role played by ADV in SPNA UOHC, and the remainder of this paper will focus on the origins and impacts of predictable ADV signals. As noted above, the absence of realistic SPNA variability in the CESM-LE ensemble (Fig. 1) indicates that high CESM-DPLE skill cannot be explained by the model response to time-varying external radiative forcings (greenhouse gases, aerosols, etc.). It could be the case that the CESM response to those forcings is flawed, and that the FOSI-derived initial conditions used in CESM-DPLE do in fact contain externally-forced variations that contribute significantly to initialized decadal prediction skill. Regardless of the origin of the information contained in the initial conditions (external forcing versus intrinsic variability), a strong conclusion is that, in this prediction system, SPNA skill derives primarily from initialization rather than the coupled model response to external forcing.

The potential predictability of the SPNA heat budget is assessed by correlating CESM-DPLE tendency terms with those from FOSI in Fig. 5. Very high pentadal skill ($r > 0.6$) is found for all budget terms north of ~ 40° N, in a zonal swath extending from the North American coast into the central and eastern SPNA. The region of highest

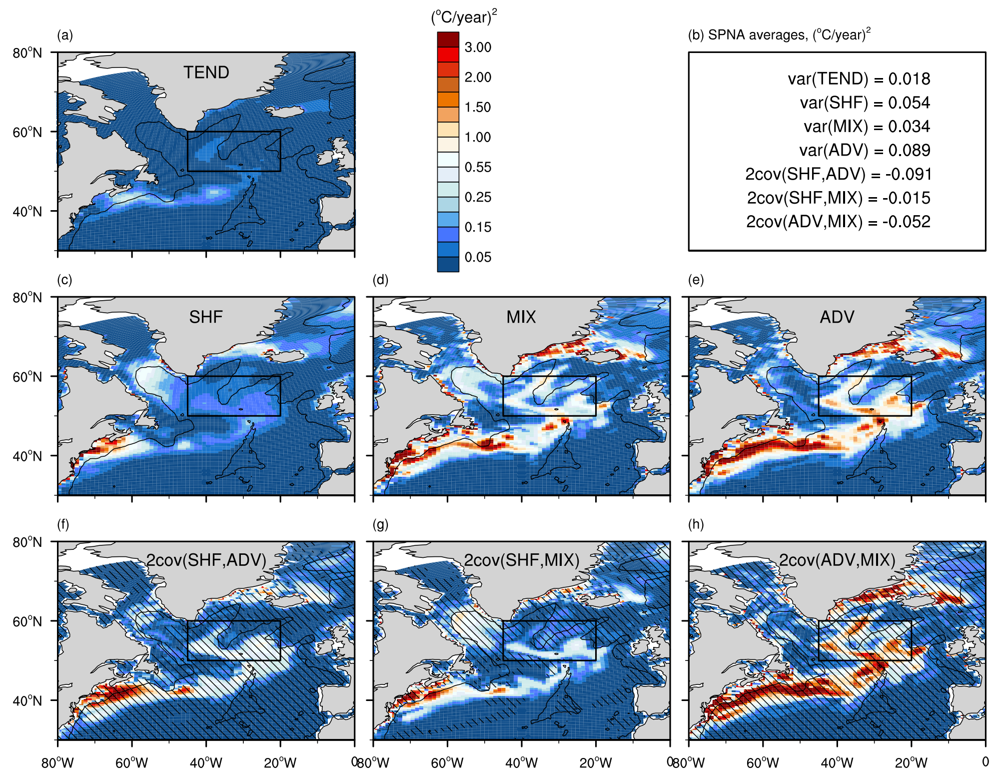


**Fig. 4** Same as Fig. 3 except all budget terms have been low-pass filtered with a Lanczos smoother with cutoff period of 60 months prior to variance computation. Note that the variances listed in (**b**) correspond to the time series plotted in Fig. 2

correlation skill coincides with the region where ADV dominates UOHC tendency on multi-year timescales (cf. Fig. 4e). This suggests that the coherent patterns of high extratropical skill seen in SHF, MIX, ADV, and TEND are ultimately driven by the ADV term. Additional evidence will be shown below that bolsters this interpretation. It is remarkable that correlation scores exceeding 0.8 are seen for each of SHF, MIX, and ADV in the region above the MAR (around 50° N, 30° W), even out to LY5-9. The skill for individual budget terms is generally higher than that for the net UOHC tendency at any given lead time, but the TEND skill is very high ($r > 0.6$) throughout the extratropics in the first pentad of prediction and it remains significant in the eastern SPNA even at LY5-9. The high skill at predicting SPNA UOHC tendency years in advance is what explains both the stability of UOHC skill metrics with lead time (Fig. 1) and the large skill improvement over damped persistence in this region (Yeager et al. 2018). The subtropical heat budget skill is generally more short-lived than in the extratropics for each of the terms, but a swath of significant, persistent tendency skill is found between the west coast of Africa and the Caribbean (Fig. 5k). This feature can perhaps be interpreted as a manifestation of the subtropical limb of the Atlantic Multidecadal Variability (AMV) pattern, which has been shown to be at least partly driven by ocean dynamics in the SPNA in the CESM model (Kim et al. 2020).

The relative magnitude of heat budget signals in the prediction ensemble (quantified as $\sqrt{PVF}$; see Fig. ES4 in Online Resource 1) exhibits a close match to FOSI correlation skill (Fig. 5) throughout much of the GS/NAC and eastern SPNA regions. However, $\sqrt{PVF}$ is considerably higher at far northern latitudes and in the subtropics. This mismatch is easily seen as regions where RPC (see Eq. 2) is significantly less than one in Fig. 6. Low ensemble spread in CESM-DPLE indicates that there is higher potential predictability in those regions than is realized in practice, even when verifying against FOSI (which employs the same ocean and sea-ice models as CESM-DPLE). Of particular note is the rapid loss of SHF and MIX skill (but not PVF) in the Labrador Sea (see LY1-5 in Figs. 5, 6), a region where those two terms dominate the FOSI budget (Fig. 4). The PVF maps suggest that 25% or more of the variance in SHF and MIX in the Labrador Sea (as well as in the Irminger and Norwegian Seas) is predictable variance even out to LY5-9 (Fig. ES4). This implies that the atmosphere in CESM-DPLE has noteworthy signal variance for heat budget forcing in high latitude regions of deep water mass formation, but it is not skillful variance insofar as it differs from the reanalysis used to drive FOSI. This further implies that

**Fig. 5** Upper ocean (to 295 m) heat budget predictability for lead years: 1–5 (left panels), 3–7 (middle panels), and 5–9 (right panels). Rows (from top to bottom) show anomaly correlation coefficients between CESM-DPLE and FOSI for: SHF, ADV, MIX, and TEND, respectively. Stippling indicates correlations that are not statistically significant. Thin black contour shows the 2500 m isobath. All timeseries were detrended prior to analysis

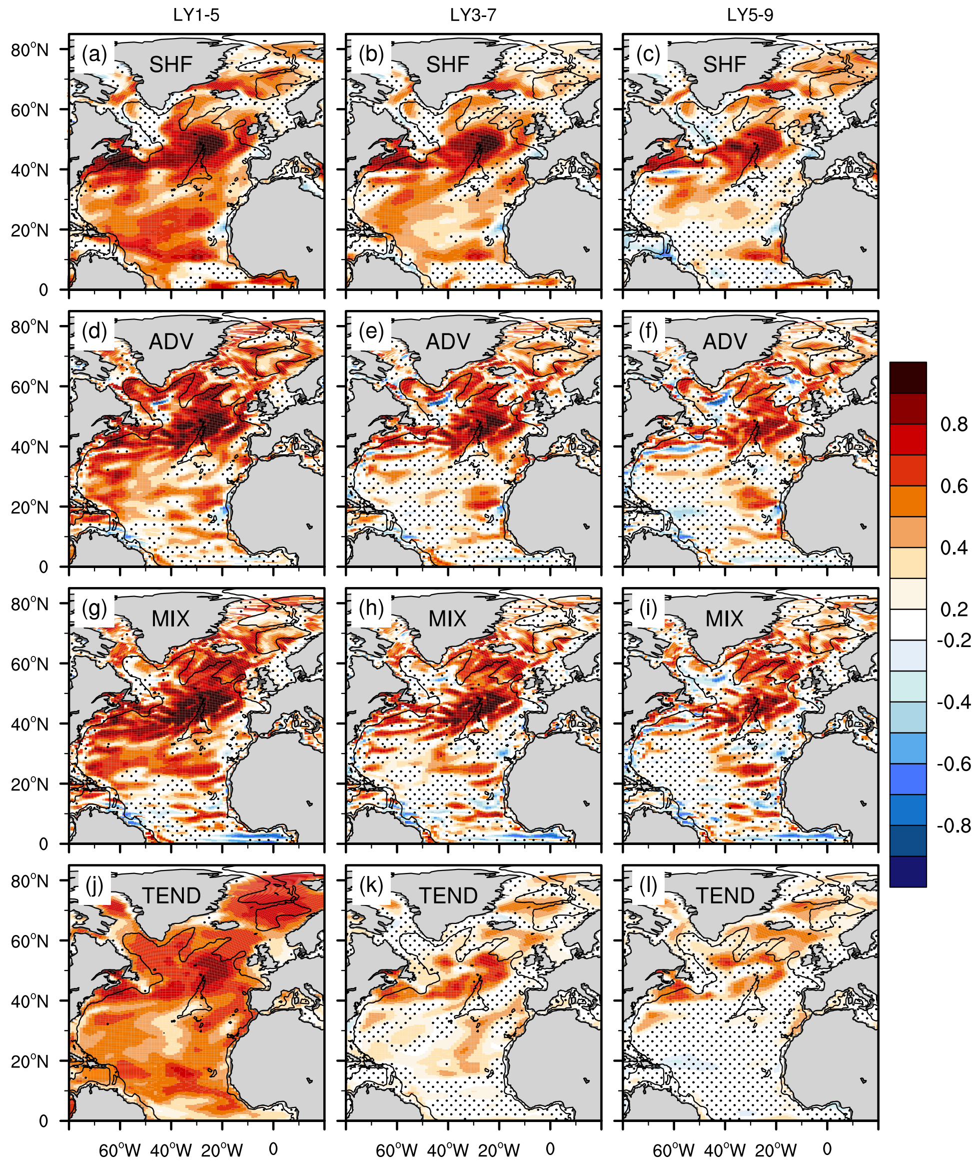


there may be ways to improve prediction of North Atlantic deep water formation through focused work to understand the origins of unrealistic atmospheric signals over these key regions. The relatively high PVF (significantly low RPC) over the high latitude deep water formation regions is likely part of the explanation for the relatively high PVF seen for SPNA UOHC (Fig. 1; $\sqrt{PVF}$ always exceeds correlation scores).

## 3.2 The abyssal mechanisms that sustain subpolar Atlantic skill

What accounts for the high and persistent advective heat convergence skill in the central SPNA in CESM-DPLE? The UOHC tendency skill would appear to be related to very high and long-lasting skill (r ~ 0.8 for LY5-9) at predicting low-frequency variations in net, column-integrated meridional heat transport (MHT) in the extratropical band 40° N– 60° N (Fig. 7c). However, the skill is much lower and shorter-lived for $AMOC_{max}$ than for MHT in that latitude band (Fig. 7b), suggesting that the ocean dynamical memory relevant to SPNA heat convergence and UOHC skill is not directly related to AMOC strength. It is interesting that low ensemble spread would imply much higher higher predictability for AMOC at all latitudes than is realized in practice when verifying against the FOSI observational proxy (Fig. 7a, b). This would appear to relate to the low RPC over deep water formation regions noted above. It seems that the prediction system has high confidence in its predictions of AMOC surface forcing out to decadal lead times, but this common (across ensemble members) forcing signal is not realistic, and so AMOC skill drops rapidly. The

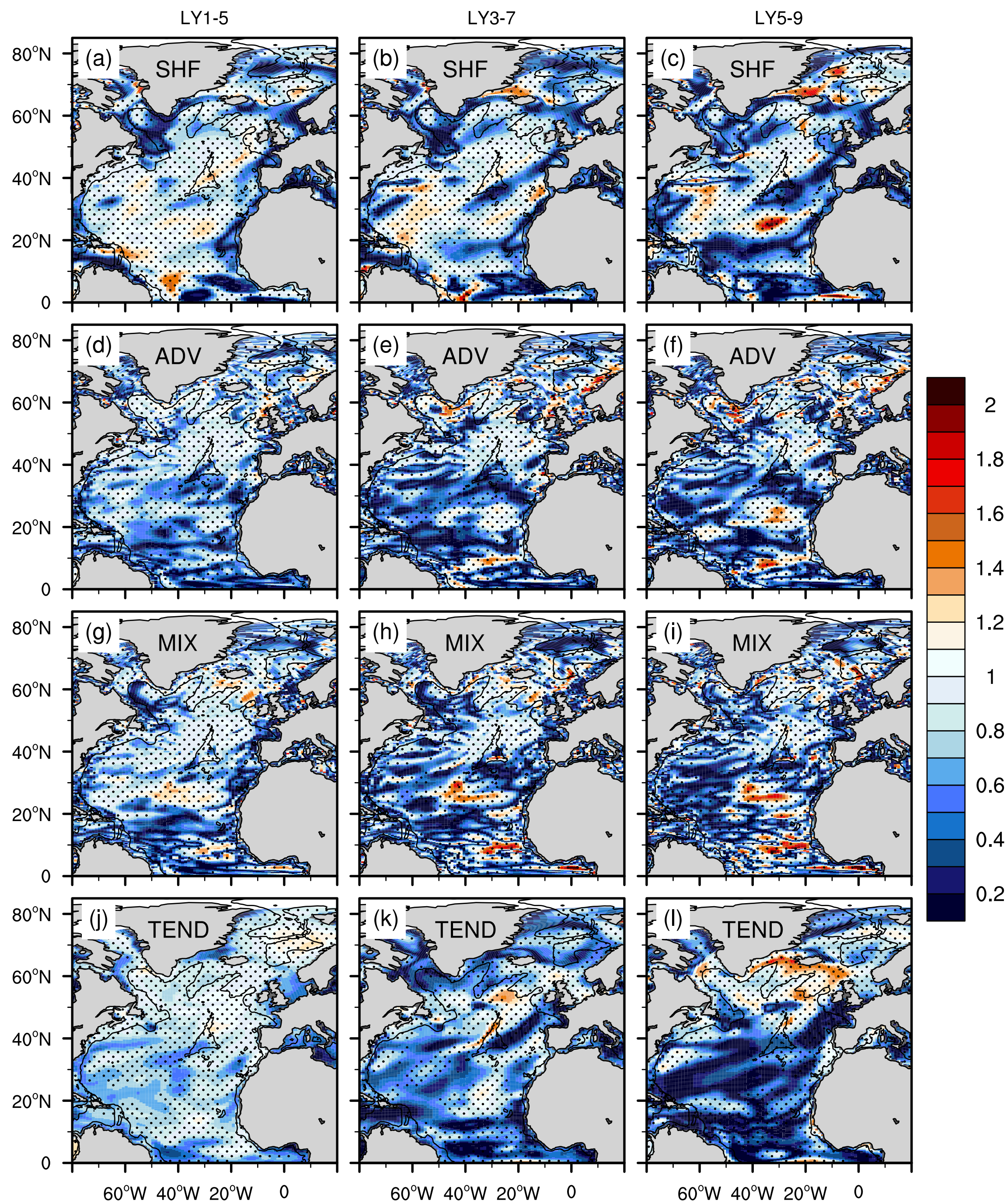


**Fig. 6** Ratio of predictable components (RPC; see Sect. 2.3.1 for details) for UOHC budget for lead years 1–5 (left panels), 3–7 (middle panels), and 5–9 (right panels). Rows (from top to bottom) show RPC for: SHF, ADV, MIX, and TEND, respectively. Stippling indicates RPC values that are not significantly different from 1. Thin black contour shows the 2500 m isobath. All timeseries were detrended prior to analysis

same is true for MHT, except in the extratropical band where MHT skill is commensurate with (only slightly lower than) that implied by the PVF (Fig. 7c, d). The skill at predicting FOSI MHT degrades quickly for latitudes south of ~ 40° N, which likely contributes to the low UOHC budget skill in the subtropical gyre seen in Fig. 5, but the stable MHT skill in the extratropics suggests that MHT in this band is largely immune to the degradations in surface forcing skill that cause AMOC skill to drop.

When viewed in full depth-latitude space, it is apparent that there is in fact very high skill at predicting variations in deep (below 2500 m) overturning in the extratropics

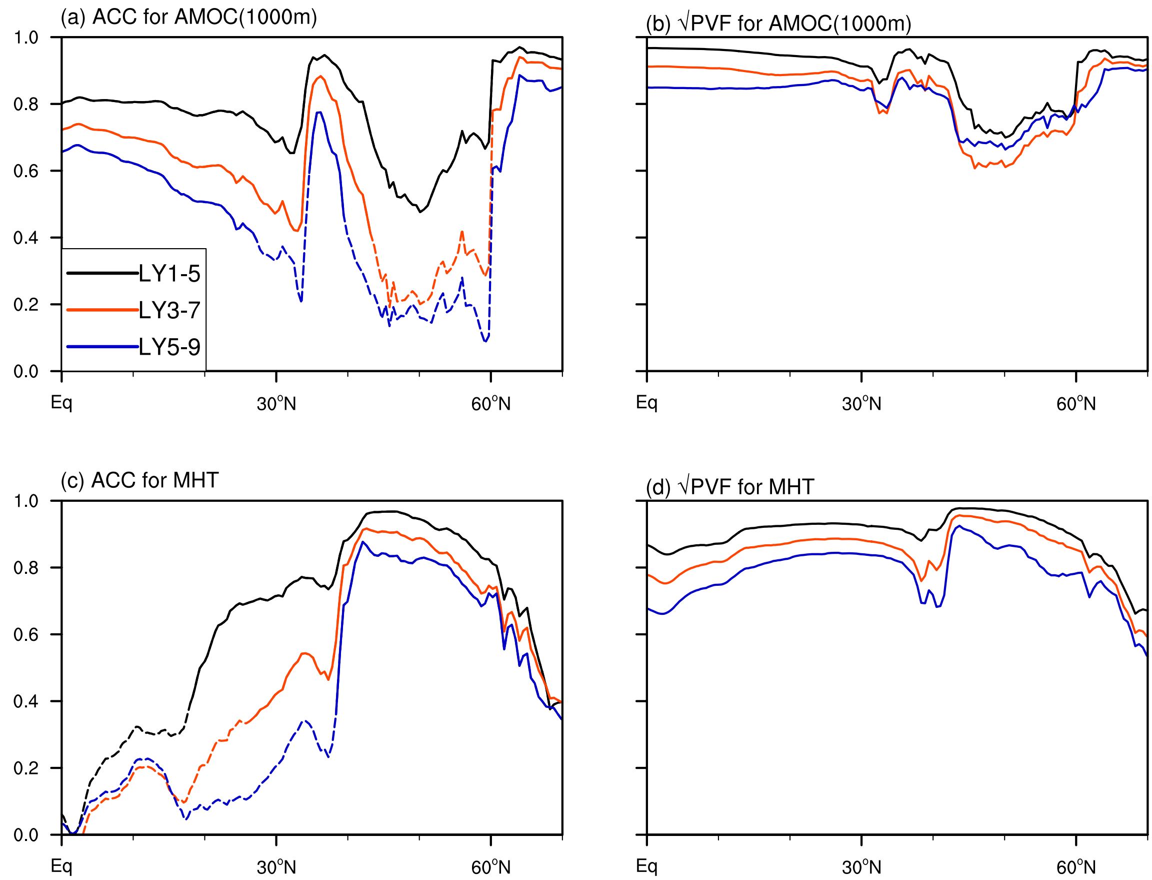


**Fig. 7** Anomaly correlation as a function of latitude between CESM-DPLE and FOSI for eulerian-mean **a** AMOC at 1000 m depth and **c** Atlantic meridional heat transport (MHT), for lead years: 1–5, 3–7, and 5–9. Right panels (**b**, **d**) show corresponding values for the square root of PVF. Statistically significant correlations (left panels) are indicated by solid curves. All time series were detrended prior to analysis

(Fig. 8a–c). This is missed when focusing on indices intended to reduce AMOC to a single value as a function of latitude (as in Fig. 7). The spatial distribution of PVF for AMOC(z) also indicates that the abyssal overturning circulation has exceptionally high signal-to-noise within the CESM-DPLE ensemble (Fig. ES5 in Online Resource 1). How does high predictability of abyssal flow translate into predictable MHT, and in particular, predictable advective heat convergence in the near surface ocean? The answer relates to the topographic coupling of the thermohaline overturning and gyre circulations described in Yeager (2015) and expounded upon below.

There is very high and long-lasting skill at predicting BSF variations in the extratropical band (Fig. 9a–c), particularly along the GS/NAC pathway discussed above. Maximum BSF skill is found to the east of the Grank Banks around 45° N on the western flank of the MAR, extending northeastward to the Rockall Plateau. This region of remarkably high decadal prediction skill ($r > 0.9$ in Fig. 9a–c) corresponds precisely to the region of strong, decadal, buoyancy-driven BSF variance highlighted and explained in Yeager (2015). Abyssal flow interaction with bottom bathymetry generates barotropic vortex stretching that can drive the gyre from below in the same way that wind stress curl forcing drives the gyre from above. These barotropic dynamics are reflected in variations of vertical velocity at the ocean bottom:

$$w_{bot} = -\mathbf{v} \cdot \nabla H \tag{6}$$

where $\mathbf{v}$ is the horizontal bottom velocity and $H$ is ocean depth. Pentadal variations in $w_{bot}$ are highly predictable (Fig. 9j–l), particularly on the slopes of the MAR where $\nabla H$ is large (see bathymetry map in Fig. ES1 in Online Resource 1), but with high skill extending all the way into the subtropics. North of ~ 40° N, this predictable $w_{bot}$ forcing translates into predictable barotropic gyre circulation. Consistent with this barotropic mechanism, we find that SSH is also highly predictable along the GS extension, on either side of the MAR around 45°N, and into the eastern SPNA (Fig. 9g–i). Again, this is consistent with earlier work showing that FOSI SSH variability in these regions is largely decadal

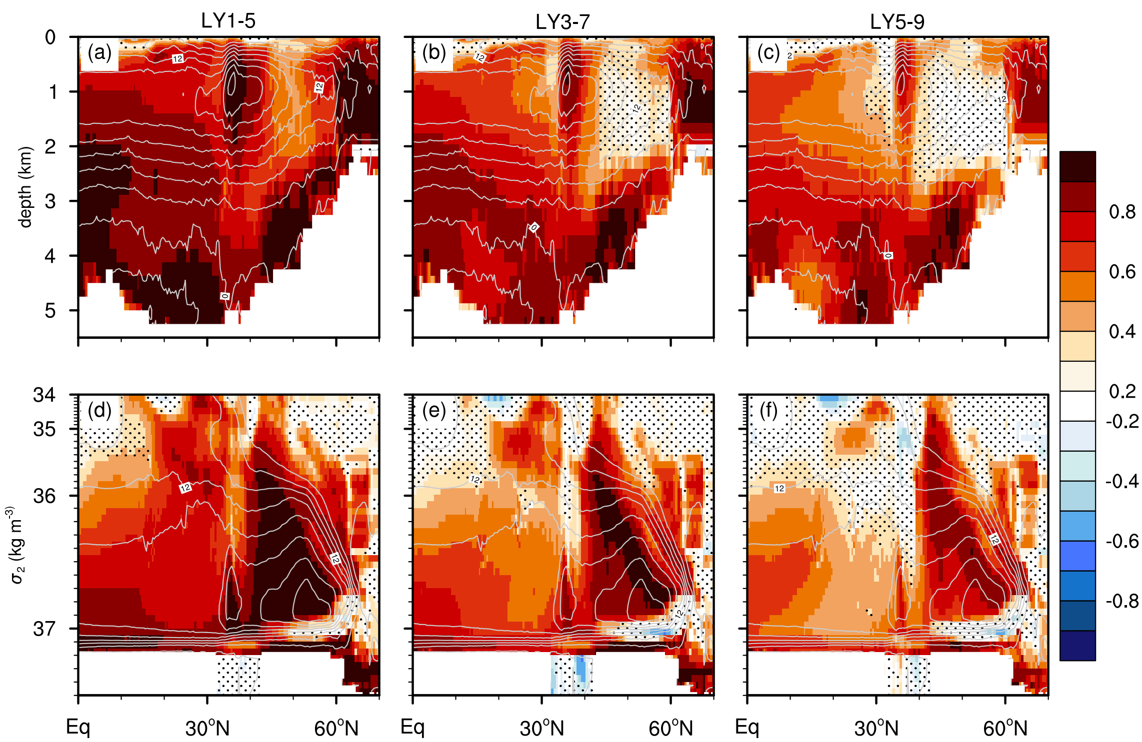


**Fig. 8** AMOC predictability for lead years: 1–5 (left panels), 3–7 (middle panels), and 5–9 (right panels). Rows (top and bottom) show anomaly correlation coefficients between CESM-DPLE and FOSI for: AMOC(z) and AMOC($\sigma_2$), respectively. Stippling indicates correlations that are not statistically significant. Grey contours show the climatological AMOC streamfunctions from FOSI (contoured at 3 Sv intervals). All timeseries were detrended prior to analysis

and buoyancy-driven (Yeager and Danabasoglu 2014). The predictability of SSH (and in particular, SSH gradients in the vicinity of the MAR) is an important contributor to predictable upper ocean advective heat convergence in the central and eastern SPNA discussed above (Fig. 5d–f) and further elucidated below (Fig. 11).

The fundamental source of ocean decadal memory in CESM-DPLE in the North Atlantic is slow, interior propagation of long-lived LSW thickness anomalies. Exceptionally predictable, abyssal thickness anomalies (Fig. 9d–f; see Sect. 2.3.3 for definition) are what underpin the very high SPNA predictability in the fields discussed above: abyssal circulation, $w_{bot}$, BSF, SSH, ADV, TEND, and UOHC. The NAO-related formation and interior propagation of LSW thickness anomalies, and their surface manifestation as low-frequency variations in the extratropical SSH field, is clearly evident in an animation of monthly FOSI anomalies spanning 1958–2017 (see Online Resource 2). The animation shows that $\Delta z_{LSW}$ signals generated in the interior Labrador Sea follow several pathways after exiting that region. Some propagation of thickness signal is evident along the western boundary, but the largest anomalies tend to follow eastward, interior pathways towards the MAR, whereupon they recirculate within the SPNA or split into branches that infiltrate southward on either side of the MAR. It appears that the interior pathways are most important for inducing large BSF and SSH anomalies relevant to CESM-DPLE predictability. In particular, the southward interior pathway towards the western flank of the MAR results in accumulation of large $\Delta z_{LSW}$ anomalies that get blocked by bathymetry and persist for years.

Figure 10 displays a snapshot from the animation showing a persistent blob of anomalously thick LSW sitting on the western flank of the MAR that resulted from very anomalous LSW production in the early 1990s. The large, positive $\Delta z_{LSW}$ anomaly is associated with large negative/positive SSH anomalies on the western/eastern flanks of the MAR (Fig. 10a). This anomalous SSH gradient contributes to anomalous northward heat transport into the central and eastern SPNA in the upper ocean and an associated (predictable) positive ADV signal in the late 1990s (Figs. 2, 5). The time series of anomalous meridional geostrophic flow averaged over the MAR ($v_{MAR}$; see Sect. 2.3.4) is shown in panel c of Figure 10. The CESM-DPLE shows excellent skill at predicting this SSH-driven flow out to decadal lead times (LY5-9 plotted), and the high predictability relates to the fact that SSH in this region is predominantly buoyancy-forced (ie., it reflects the steric effect of deep water mass anomalies). The variability of $\Delta z_{LSW}$ in the western half of the MAR box

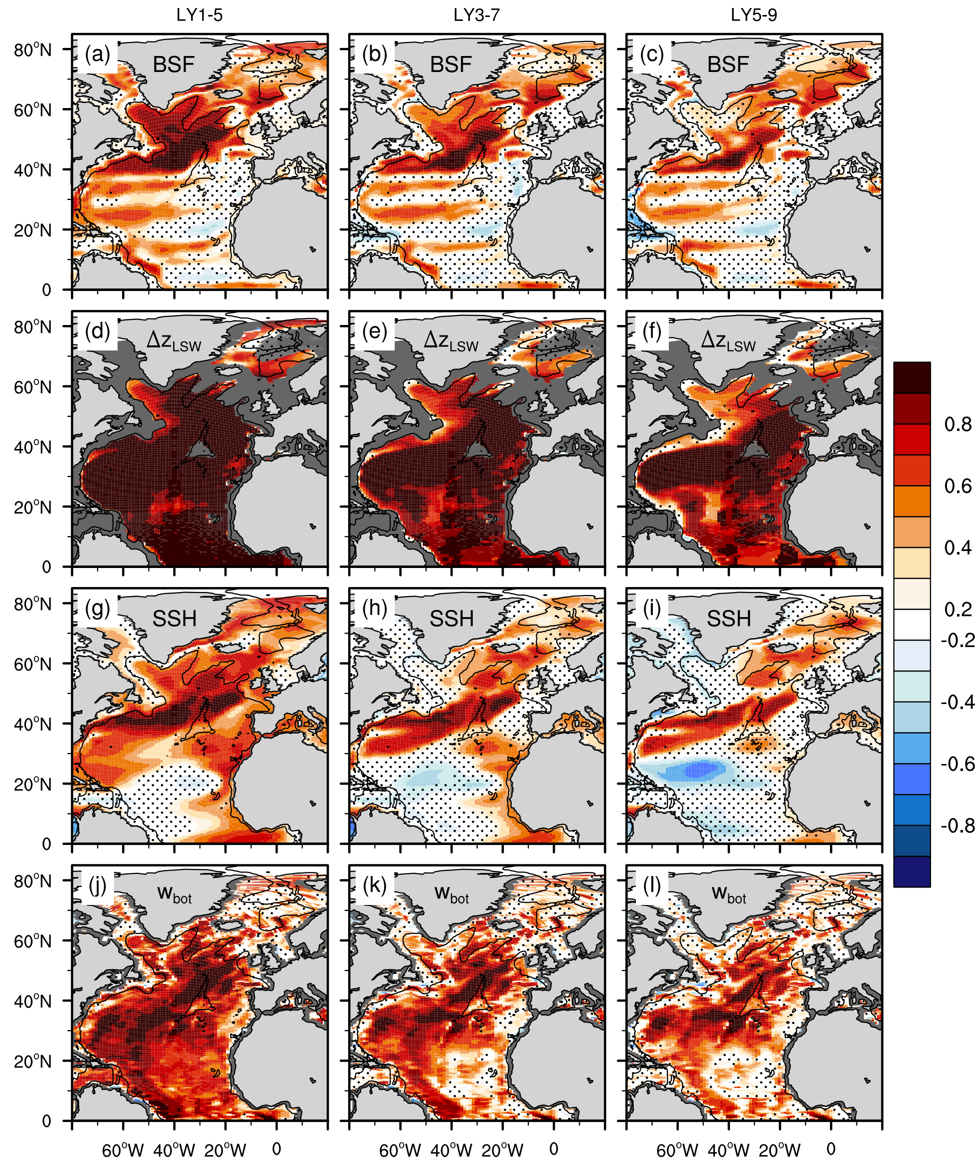


**Fig. 9** Predictability of the buoyancy-driven gyre circulation for lead years: 1–5 (left panels), 3–7 (middle panels), and 5–9 (right panels). Rows (top to bottom) show anomaly correlation coefficients between CESM-DPLE and FOSI for: BSF, $\Delta z_{LSW}$, SSH, and $w_{bot}$, respectively. Stippling indicates correlations that are not statistically significant. Thin black contour shows the 2500 m isobath. All timeseries were detrended prior to analysis

(Fig. 10b) is clearly correlated with the zonal SSH gradient in both FOSI and CESM-DPLE (r = 0.99 when $\Delta z_{LSW}$ leads $v_{MAR}$ by 4 years in FOSI). Thickness variations on the order of hundreds of meters in the abyssal ocean drive SSH variations on the order of centimeters in this region, with a several year time lag that will require further study to understand. Given the roughly 4 year time lag diagnosed from FOSI, it can be surmised that the near perfect prediction skill for $\Delta z_{LSW}$ early in the hindcasts (Fig. 10b, showing LY1-5) underpins the high prediction skill for $v_{MAR}$ later in the hindcasts (Fig. 10c, showing LY5-9). The evidence of LSW-driven SSH gradients combined with extraordinarily high prediction skill for $\Delta z_{LSW}$ in the vicinity of the MAR (Figs. 9, 10) leave little doubt that persistent abyssal water mass anomalies play a key role in the success of CESM-DPLE in the subpolar North Atlantic.

The positive peak in $v_{MAR}$ around the year 2000 (Fig. 10c) occurs several years after the 1996 peak in SPNA UOHC tendency (Fig. 2) that led to the abrupt, mid-1990s SPNA warming, and so the timing of signals linked to SSH-driven flow anomalies over the MAR requires some clarification. The temporal sequence of events associated with predictable SPNA UOHC change (dominated by the mid-1990s event) is summarized in Fig. 11, which shows FOSI heat budget regressions onto the normalized $v_{MAR}$ time series (black curve in Fig. 10c). The associated correlation maps are provided in Figure ES9 (online Resource 1) using a t-test for statistical significance after taking into account temporal autocorrelation (Bretherton et al. 1999). Advective heat convergence (ADV) in the central and eastern SPNA maximizes in sync with $v_{MAR}$ (Fig. 11, lead 0), but the net UOHC tendency (TEND)

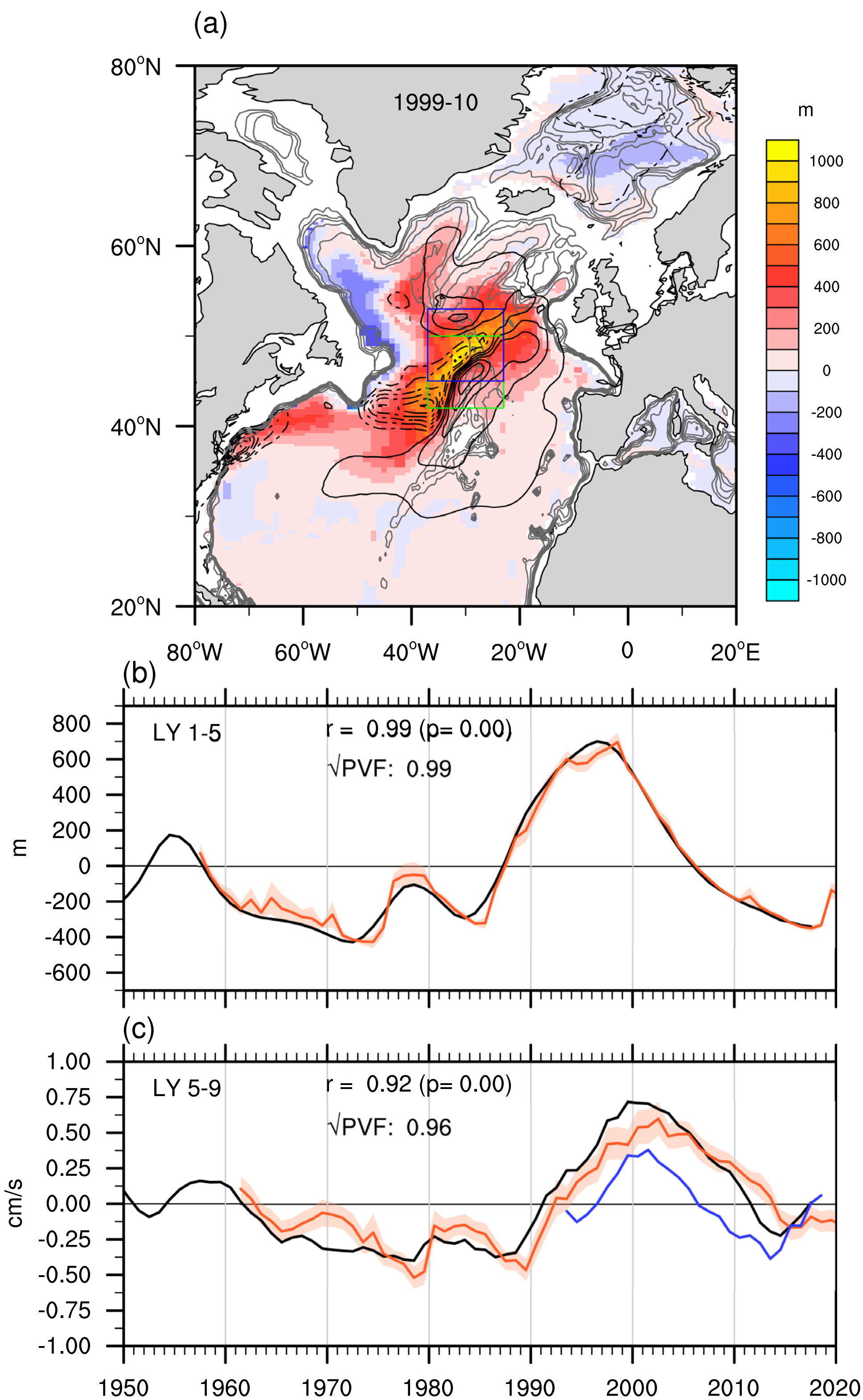


**Fig. 10** **a** LSW thickness ($\Delta z_{LSW}$) anomaly (color fill) from October 1999 overlaid by low-pass filtered (Lanczos smoother with cutoff period of 60 months) SSH anomaly (contoured at 2 cm intervals, omitting 0). Both fields are from the FOSI simulation (see Online Resource 2 for corresponding animation). **b** Anomalous pentadal-mean $\Delta z_{LSW}$ averaged over the western half of the (green) MAR box from FOSI (black) and CESM-DPLE (red; lead year range 1–5 plotted). **c** Anomalous pentadal-mean geostrophic meridional flow regionally-averaged over the MAR ($v_{MAR}$; refer to Sect. 2.3.4) from FOSI (black), CESM-DPLE (red; lead year range 5–9 plotted), and satellite observations (blue). The MAR box used for observations in **c** (blue box) is shifted slightly north of that used for model fields (green box). The shading around CESM-DPLE curves represents ensemble uncertainty ($\pm 1\sigma$). Correlations (and corresponding p-values) are given for CESM-DPLE verified against FOSI, which can be compared to the square root of the predictable variance fraction ($\sqrt{PVF}$; see Sect. 2.3.1)

in that region maximizes about 4 years earlier (Fig. 11, lead − 4), as noted above. The explanation for this can be seen in the corresponding regressions for MIX and SHF, whose spatial patterns clearly mirror the ADV signals over the MAR and SPNA but act to damp the ADV tendency. As the ADV signal grows over the MAR and begins to extend northward and eastward into the SPNA (Fig. 11, leads − 8 to 4), MIX and SHF play catch up and can only

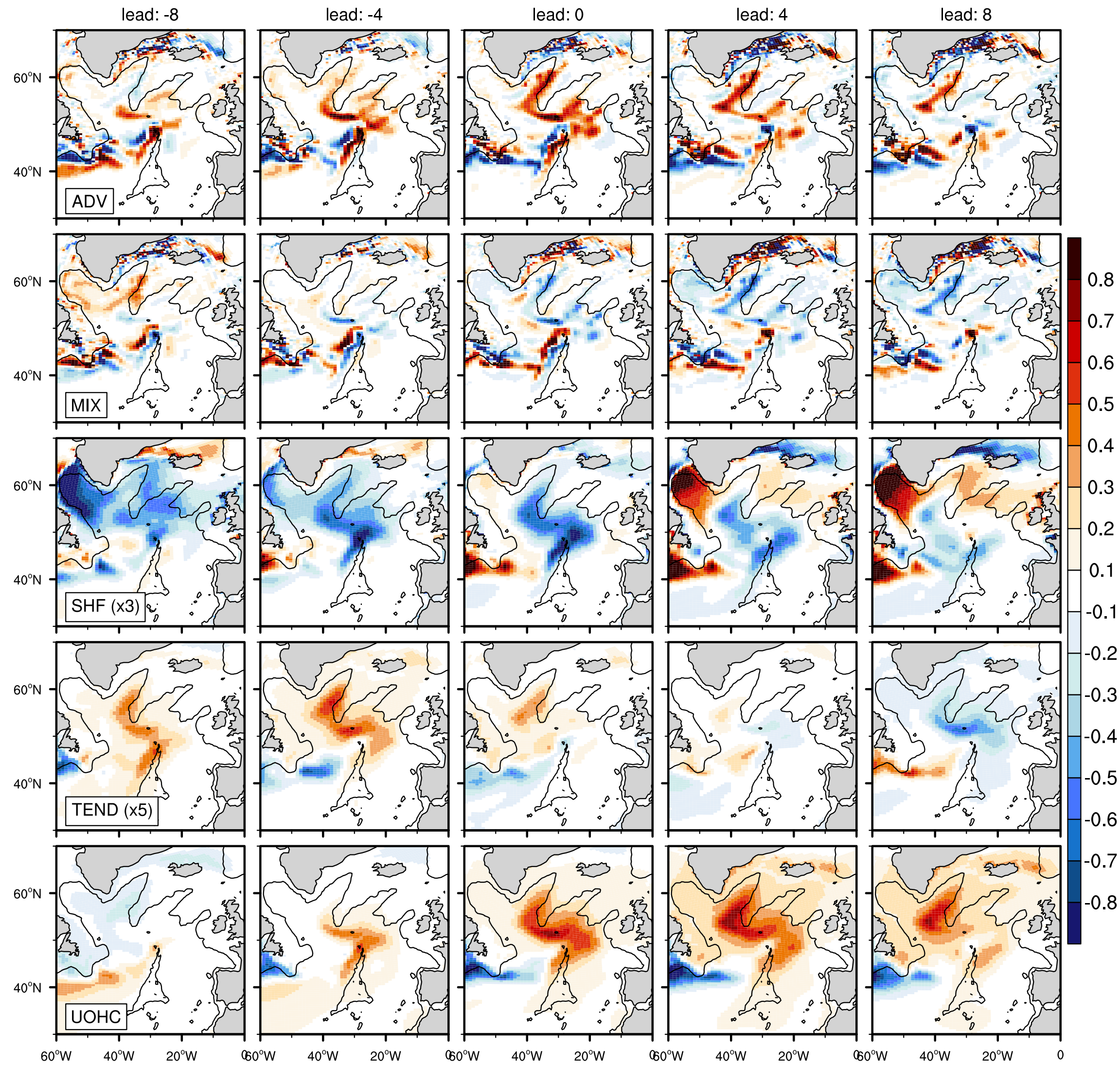


**Fig. 11** FOSI heat budget regressed onto (normalized) geostrophic meridional flow anomalies regionally-averaged over the MAR ($v_{MAR}$; black curve in Fig. 10c): (top row) ADV, (second row) MIX, (third row) SHF (multiplied by a scale factor of 3), (fourth row) TEND (multiplied by a scale factor of 5), (fifth row) UOHC. All time series were detrended and smoothed with a running 5-year boxcar filter prior to regression. Columns show results for different lead times in years with $v_{MAR}$ leading/lagging for positive/negative lead times such that advancing from left to right shows the progression through time. Units for top 4 rows is (°C/year)/(std. dev.); units for bottom row is °C/(std. dev.)

fully counter the ADV signal by about lead 4 (4 years after the $v_{MAR}$ maximum, when TEND is near zero). The largest discrepancy between ADV and (MIX+SHF), and hence maximum in TEND, occurs at lead − 4 (ie, 1996 in historical terms), which results in a dramatic UOHC change from lead − 4 to lead 0 (noting that the UOHC signal is the time integral of TEND). As seen previously in Figs. 2 and 4, both MIX and SHF are smaller terms than ADV in the SPNA, but they work together to counter buoyancy-driven ADV anomalies. The high predictability of the SPNA heat budget over the MAR and SPNA (Fig. 5), including MIX and SHF terms, arises from the ability to skillfully predict $\Delta z_{LSW}$, $v_{MAR}$, and the associated evolution of FOSI heat budget terms depicted in Fig. 11.

## 4 Discussion

The predictability dynamics at work in CESM-DPLE are barotropic insofar as the critical ocean heat transport (and transport convergence) skill appears to be maintained by multi-year skill at predicting the gyre circulation and dynamic height field in the intergyre region between the subtropical and subpolar Atlantic. Bottom vortex stretching is the relevant (barotropic) forcing term that sustains the predictable gyre circulation. Persistent LSW thickness anomalies represent the essential core of ocean memory, driving predictable anomalous bottom flow (with associated $w_{bot}$ and BSF signals) as well as anomalous surface flow through steric SSH change. The analysis of deep density signals in terms of water mass thickness permits a transparent linkage between surface water mass formation, interior propagation, and surface expression in the SSH field that dictates upper ocean geostrophic flow.

The net strength of depth-space AMOC exhibits much lower skill than the net heat transport north of 40°N (Fig. 7), suggesting that its importance for decadal prediction is not as high as is commonly assumed. Low AMOC(z) skill (Figs. 7, 8) is presumably related to the rapid loss of skill at predicting high latitude surface forcing (Fig. 5a–c) and associated LSW formation and thickness changes within the Labrador Sea (Fig. 9d–f). Poor prediction of the wind-driven component of extratropical AMOC variability is likely a compounding factor (not shown). The rapid transmission down the western boundary of (erroneous) LSW thickness signals results in a relatively quick loss in skill at predicting western boundary density anomalies that set AMOC(z) strength through the thermal wind relation. Note that the LY1-5 skill for AMOC(z) at 45° N (r ≈ 0.6; Fig. 7a) is not far off from the multi-model AMOC skill reported in Pohlmann et al. (2013), so it would not appear that AMOC(z) is less predictable in CESM-DPLE than in other systems. The emphasis here, though, is the contrast between this short-lived AMOC(z) skill and the much longer-lasting MHT skill at extratropical latitudes (Fig. 7c).

It is not clear how to reconcile these results with earlier work that emphasizes the role of the overturning component of ocean heat transport in skillful SPNA prediction (e.g., Robson et al. 2012; Msadek et al. 2014; Robson et al. 2017). One possible explanation is that these prior works focus on select case studies of rapid SPNA change rather than skill averaged across all initialization dates. Another is that fundamentally different mechanisms could be at work in the different prediction systems. The analysis of sigma-space AMOC skill suggests that there might in fact be no discrepancy at all. When viewed in density coordinates (Fig. 8d–f), there is high skill at predicting the strength of both shallow and deep circulations even out to LY5-9 in the extratropical band (40° N–60° N). There is a rapid loss of AMOC($\sigma_2$) skill in the lightest class of southward flowing water, which corresponds to the surface Labrador Current and its southward extension along the shelf of the Grand Banks, and this loss of skill at predicting the near-surface western boundary current would appear to be related to the rapid loss of AMOC(z) skill. However, the skill is very high for southward flow in the abyssal layers ($37.1 \leq \sigma_2 \leq 37.2$ kg m$^{-3}$) which corresponds to the densest LSW water and even denser overflow waters. There is another band of very high skill (r > 0.8) in the warm (light), northward-flowing, extratropical branch of AMOC($\sigma_2$). A key thesis of this study is that the high skill of the northward flowing branch in Fig. 8d–f *derives from* the skill in the abyssal layer. In other words, the AMOC($\sigma_2$) perspective predominately reflects horizontal barotropic gyre dynamics north of about 40° N (Zhang 2010; Kwon and Frankignoul 2014). The strong covariance between bottom and surface flows discussed in Sect. 3.2 manifests as bands of high predictive skill in the lower and upper branches of AMOC($\sigma_2$) between 40° N–60° N, separated by a band of very low skill centered around $\sigma_2 = 37.0$ kg m$^{-3}$ (Fig. 8). It follows that geometric decompositions of heat transport (Bryan et al. 1975) will show a significant (and predictable) overturning component even in the extratropical band insofar as there is high skill at predicting anomalous transport of northward-flowing (warm) surface water and southward-flow (cold) deep water. As we have shown, however, the relation between heat transport and volumetric overturning is rather subtle, and AMOC(z) is less relevant than AMOC ($\sigma_2$) for understanding SPNA predictability dynamics. This is because the latter better reflects the topographically-coupled overturning/gyre dynamics that factor significantly in SPNA ocean heat transport (Yeager 2015).

A novel result is the important role played by the Mid-Atlantic Ridge (MAR) in SPNA predictability. In CESM-DPLE, the MAR acts like a dam that obstructs the interior propagation of deep water mass anomalies. As a consequence, consecutive episodes of anomalous LSW formation result in the growth of a quasi-stationary thickness anomaly on the western flank of the MAR. This in turn induces persistent BSF, SSH, and MHT anomalies. The geographical proximity of the MAR to the Labrador Sea therefore suggests an inherent limit of SPNA predictability. The interior propagation (and accumulation) of pre-formed LSW thickness anomalies is exceptionally predictable (see Figs. 9d–f, 10), but there is much less skill at predicting the formation of LSW thickness anomalies (see Fig. 9d–f in the Labrador Sea). By LY5-9, the low skill at predicting water mass formation results in a propagation of low $\Delta z_{LSW}$ skill almost all the way to the MAR. It can be surmised that the ability to predict MHT in the extratropical band (Fig. 7c), and ADV, SHF, and MIX in the central/eastern SPNA (Fig. 5), would quickly degrade once the LSW thickness skill on the western flank of the MAR disappears. Longer hindcasts would be needed to test this hypothesis.

The fidelity of the predictability mechanism at work in CESM-DPLE remains an open question that cannot be fully addressed in the present work. The demonstrated decadal skill of this system when verified against SPNA observations of UOHC (Figs. 1, ES3) and SST (Yeager et al. 2018), as well as atmospheric fields such as NAO and winter blocking frequency (Athanasiadis et al. 2020), suggests that the

CESM-DPLE mechanisms underpinning SPNA UOHC prediction skill are probably not entirely unrealistic despite the many model flaws. Satellite observations of dynamic sea level, while too short to permit full validation of the simulated multidecadal variability in the SPNA, do offer some confirmation that simulated low-frequency changes in meridional surface geostrophic flow over the MAR are realistic (Fig. 10c). Maps of low-pass filtered annual surface geostrophic flow computed from FOSI SSH and altimetry (Fig. ES7,8 in Online Resource 1) show some common features, such as the development of persistent, positive northward flow anomalies above the MAR the late 1990s and early 2000s, presumably the result of vigorous LSW production in early 1990s. On the other hand, this comparison also reveals that FOSI SSH anomalies are too large (evident also from Fig. 10c), which may relate to the overproduction of LSW in the CESM model (Li et al. 2019) and may in turn help explain the unrealistically large SPNA UOHC variance in FOSI (Fig. 1). Preliminary analysis of a FOSI simulation using an eddy-resolving ocean configuration of CESM indicates that the essential elements of the mechanism described above (large NAO-driven LSW thickness variations that correlate with SSH as they propagate through interior pathways, particularly as they encounter the MAR) are robust (not shown). The in-depth examination of this predictability mechanism in other models, including high resolution models, will be the topic of future work.

## 5 Conclusions

The mechanisms underpinning decadal predictability of subpolar North Atlantic (SPNA) upper ocean heat content in a widely-used initialized prediction dataset, the CESM-DPLE (Yeager et al. 2018), have been explored by assessing the skill at reproducing the mechanisms at work in a well-studied, reanalysis-forced ocean—sea-ice (FOSI) simulation performed with the same model. A strength of this approach is that it leverages previous work that has revealed the dominant influence of surface buoyancy forcing and flow-bathymetry interactions on simulated SPNA dynamics (Yeager and Danabasoglu 2014; Yeager 2015). A drawback is that the question of model fidelity remains an outstanding issue that limits the strength of conclusions. A summary of key findings is as follows:

- Advective heat convergence is the dominant term in the upper ocean heat budget in the SPNA on multi-year timescales. It is a driving term that gives rise to large, coherent mixing and heat flux tendencies of opposite sign.
- CESM-DPLE shows very high potential predictability skill (as well as high actual prediction skill) for SPNA upper ocean heat content (UOHC) variations even out to 10-year lead times, with only slight degradation in the signal-to-noise across a 40-member ensemble. This skill derives from accurate multi-year prediction of heat budget tendency terms in the central and eastern SPNA. Skillful prediction of advective heat convergence in a region north of 40° N and over the Mid-Atlantic ridge appears to be the primary source of UOHC tendency skill.
- Long-lasting skill at predicting meridional heat transport at intergyre latitudes (40° N–60° N) is not explained by the strength of depth-space AMOC, because skill for AMOC(z) is quite short-lived. Instead, the critical advective heat transport skill is related to highly predictable coupled overturning/gyre dynamics. The latter manifests as long-lasting skill for the barotropic streamfunction over the MAR in the intergyre region, and for the upper and lower branches of AMOC when computed in sigma-space.
- The fundamental decadal ocean memory in the North Atlantic resides in persistent, slowly-propagating Labrador Sea Water thickness anomalies. These deep water mass anomalies drive surface advection by altering the sea surface height in the subpolar region, and they drive bottom advection by altering abyssal pressure gradients. When they propagate to regions of large bathymetric gradients (such as the MAR), they induce strong coupling between the overturning and gyre circulations.
- Satellite-based sea level measurements offer tentative support to the finding that large, decadal variations in the strength of the zonal SSH gradient over the MAR, generated by persistent LSW thickness anomalies in the abyssal ocean on the western flank of the MAR, play a critical role in SPNA predictability.

More work is clearly needed to determine whether the predictability mechanism outlined above holds true in general. The DCPP component of CMIP6 (Boer et al. 2016) will help facilitate an examination of the robustness to differences in model formulation and prediction system design. Testing the sensitivity to model resolution is more challenging, as multidecadal historical simulations using eddy-resolving ocean models are still quite rare, and initialized ensemble prediction at such resolution remains a limited, frontier activity. An exploration of the characteristics of abyssal thickness anomalies in an ocean with fully-developed mesoscale turbulence is needed and is planned. Finally, satellite-based SSH measurements are and will continue to be a crucial benchmark, but this work highlights the potential importance for surface climate of variability in the deep ocean. The lack of deep ocean observations therefore poses considerable challenges for decadal prediction initialization and mechanistic verification.

**Acknowledgements** SY acknowledges support from the National Science Foundation (NSF) Grants OPP-1737377 and OCE-1243015, as well as from the Blue-Action project (European Unions Horizon 2020 research and innovation programme, #727852). NCAR is a major facility sponsored by NSF under Cooperative Agreement No. 1852977. The CESM-DPLE was generated using computational resources provided by the National Energy Research Scientific Computing Center, which is supported by the Office of Science of the U.S. Department of Energy under Contract DE-AC02-05CH11231, as well as by an Accelerated Scientific Discovery grant for Cheyenne (https://doi.org/10.5065/D6RX99HX) that was awarded by NCAR's Computational and Information Systems Laboratory.

## References


Athanasiadis PJ, Yeager SG, Kwon Y, Bellucci A, Smith DW, Tibaldi S (2020) Decadal predictability of North Atlantic blocking and the NAO. NPJ Clim Atmos Sci 3:20. https://doi.org/10.1038/s41612-020-0120-6

Boer GJ, Kharin VV, Merryfield WJ (2013) Decadal predictability and forecast skill. Clim Dyn 41:1817–1833. https://doi.org/10.1007/s00382-013-1705-0

Boer GJ, Smith DM, Cassou C, Doblas-Reyes F, Danabasoglu G, Kirtman B et al (2016) The Decadal Climate Prediction Project (DCPP) contribution to CMIP6. Geosci Model Dev 9:3751–3777. https://doi.org/10.5194/gmd-9-3751-2016

Bretherton CS, Widmann M, Dymnikov VP, Wallace JM, Bladé I (1999) The effective number of spatial degrees of freedom of a time-varying field. J Clim 12:1990–2009

Bryan K, Manabe S, Pacanowski RC (1975) A global ocean-atmosphere climate model. Part II. The oceanic circulation. J Phys Oceanogr 5:30–46. https://doi.org/10.1175/1520-0485(1975)005<0030:AGOACM>2.0.CO;2

Buckley MW, Ponte RM, Forget G, Heimbach P (2014) Low-frequency SST and upper-ocean heat content variability in the North Atlantic. J Clim 27:4996–5018. https://doi.org/10.1175/jcli-d-13-00316.1

Buckley MW, Ponte RM, Forget G, Heimbach P (2015) Determining the origins of advective heat transport convergence variability in the North Atlantic. J Clim 28:3943–3956. https://doi.org/10.1175/jcli-d-14-00579.1

Choudhury D, Sen Gupta A, Sharma A, Mehrotra R, Sivakumar B (2017) An assessment of drift correction alternatives for CMIP5 decadal predictions. J Geophys Res Atmos 122:10282–10296. https://doi.org/10.1002/2017JD026900

Collins M, Botzet M, Carril AF, Drange H, Jouzeau A, Latif M et al (2006) Interannual to decadal climate predictability in the North Atlantic: a multimodel-ensemble study. J Clim 19:1195–1203

Danabasoglu G, Yeager SG, Bailey D, Behrens E, Bentsen M, Bi D et al (2014) North Atlantic simulations in coordinated ocean-ice reference experiments phase II (CORE-II). Part I: mean states. Ocean Model 73:76–107. https://doi.org/10.1016/j.ocemod.2013.10.005

Danabasoglu G, Yeager SG, Kim WM, Behrens E, Bentsen M, Bi D et al (2016) North Atlantic simulations in coordinated ocean-ice reference experiments phase II (CORE-II). Part II: inter-annual to decadal variability. Ocean Model 97:65–90. https://doi.org/10.1016/j.ocemod.2015.11.007

Doblas-Reyes FJ, Andreu-Burillo I, Chikamoto Y, García-Serrano J, Guemas V, Kimoto M et al (2013) Initialized near-term regional climate change prediction. Nat Commun 4:1715. https://doi.org/10.1038/ncomms2704

Downes SM, Farneti R, Uotila P, Griffies SM, Marsland SJ, Bailey D et al (2015) An assessment of Southern Ocean water masses and sea ice during 1988–2007 in a suite of interannual CORE-II simulations. Ocean Model 94:67–94. https://doi.org/10.1016/j.ocemod.2015.07.022

Eade R, Smith D, Scaife A, Wallace E, Dunstone N, Hermanson L et al (2014) Do seasonal-to-decadal climate predictions underestimate the predictability of the real world? Geophys Res Lett 41:5620–5628. https://doi.org/10.1002/2014GL061146

Farneti R, Downes SM, Griffies SM, Marsland SJ, Behrens E, Bentsen M et al (2015) An assessment of Antarctic circumpolar current and southern ocean meridional overturning circulation during 1958–2007 in a suite of interannual CORE-II simulations. Ocean Model 93:84–120. https://doi.org/10.1016/j.ocemod.2015.07.009

Fox-Kemper B, Danabasoglu G, Ferrari R, Griffies S, Hallberg R, Holland M et al (2011) Parameterization of mixed layer eddies. III: implementation and impact in global ocean climate simulations. Ocean Model 39:61–78. https://doi.org/10.1016/j.ocemod.2010.09.002 Modelling and Understanding the Ocean Mesoscale and Submesoscale

Gent PR, Mcwilliams JC (1990) Isopycnal mixing in ocean circulation models. J Phys Oceanogr 20:150–155. https://doi.org/10.1175/1520-0485(1990)020<0150:imiocm>2.0.co;2

Goddard L, Kumar A, Solomon A, Smith D, Boer G, Gonzalez P et al (2013) A verification framework for interannual-to-decadal predictions experiments. Clim Dyn. https://doi.org/10.1007/s00382-012-1481-2

Good SA, Martin MJ, Rayner NA (2013) EN4: quality controlled ocean temperature and salinity profiles and monthly objective analyses with uncertainty estimates: THE EN4 DATA SET. J Geophys Res Oceans 118:6704–6716. https://doi.org/10.1002/2013JC009067

Griffies SM, Bryan K (1997) Predictability of North Atlantic multidecadal climate variability. Science 275:181–184

Griffies SM, Biastoch A, Böning C, Bryan F, Danabasoglu G, Chassignet EP et al (2009) Coordinated ocean-ice reference experiments (COREs). Ocean Model 26:1–46. https://doi.org/10.1016/j.ocemod.2008.08.007

Griffies SM, Yin J, Durack PJ, Goddard P, Bates SC, Behrens E et al (2014) An assessment of global and regional sea level for years 1993–2007 in a suite of interannual CORE-II simulations. Ocean Model 78:35–89. https://doi.org/10.1016/j.ocemod.2014.03.004

Ilicak M, Drange H, Wang Q, Gerdes R, Aksenov Y, Bailey D et al (2016) An assessment of the Arctic Ocean in a suite of interannual CORE-II simulations. Part III: hydrography and fluxes. Ocean Model 100:141–161. https://doi.org/10.1016/j.ocemod.2016.02.004

Josey SA, Hirschi JJ-M, Sinha B, Duchez A, Grist JP, Marsh R (2018) The recent atlantic cold anomaly: causes, consequences, and related phenomena. Annu Rev Mar Sci 10:475–501. https://doi.org/10.1146/annurev-marine-121916-063102

Karspeck AR, Stammer D, Köhl A, Danabasoglu G, Balmaseda M, Smith DM et al (2015) Comparison of the Atlantic meridional overturning circulation between 1960 and 2007 in six ocean reanalysis products. Clim Dyn. https://doi.org/10.1007/s00382-015-2787-7

Kay JE, Deser C, Phillips A, Mai A, Hannay C, Strand G et al (2015) The Community Earth System Model (CESM) large ensemble project: a community resource for studying climate change in the presence of internal climate variability. Bull Am Meteorol Soc 96:1333–1349. https://doi.org/10.1175/BAMS-D-13-00255.1

Kim WM, Yeager S, Danabasoglu G (2020) Atlantic multidecadal variability and associated climate impacts initiated by ocean thermohaline dynamics. J Clim 33:1317–1334. https://doi.org/10.1175/jcli-d-19-0530.1

Kirtman B, Power SB, Adedoyin AJ, Boer GJ, Bojariu R, Camilloni I et al (2013) Near-term climate change: projections and predictability. Cambridge University Press, Cambridge. Climate Change 2013: the physical science basis. Contribution of working group

I to the fifth assessment report of the intergovernmental panel on climate change, chap. 11
Kwon Y-O, Frankignoul C (2014) Mechanisms of multidecadal Atlantic meridional overturning circulation variability diagnosed in depth versus density space. J Clim 27:9359–9376. https://doi.org/10.1175/JCLI-D-14-00228.1
Langehaug HR, Rhines PB, Eldevik T, Mignot J, Lohmann K (2012) Water mass transformation and the North Atlantic current in three multicentury climate model simulations. J Geophys Res Oceans. https://doi.org/10.1029/2012JC008021
Large WG, Nurser AG (2001) Chapter 5.1 ocean surface water mass transformation. In Siedler G, Church J, Gould J. (eds) Ocean Circulation and Climate, vol 77 of International Geophysics. Academic Press, pp 317 – 336. https://doi.org/10.1016/S0074-6142(01)80126-1
Large WG, Yeager SG (2004) Diurnal to decadal global forcing for ocean and sea-ice models: the data sets and flux climatologies. NCAR technical note NCAR/TN-460+STR. https://doi.org/10.5065/D6KK98Q6
Large WG, Yeager SG (2009) The global climatology of an interannually varying air-sea flux data set. Clim Dyn 33:341–364. https://doi.org/10.1007/s00382-008-0441-3
Li F, Lozier MS, Danabasoglu G, Holliday NP, Kwon Y-O, Romanou A et al (2019) Local and downstream relationships between labrador sea water volume and North Atlantic meridional overturning circulation variability. J Clim 32:3883–3898. https://doi.org/10.1175/jcli-d-18-0735.1
Msadek R, Delworth TL, Rosati A, Anderson W, Vecchi G, Chang Y-S et al (2014) Predicting a decadal shift in North Atlantic climate variability using the GFDL forecast system. J Clim 27:6472–6496. https://doi.org/10.1175/JCLI-D-13-00476.1
Müller WA, Baehr J, Haak H, Jungclaus JH, Kröger J, Matei D et al (2012) Forecast skill of multi-year seasonal means in the decadal prediction system of the Max Planck Institute for Meteorology. Geophys Res Lett. https://doi.org/10.1029/2012GL053326
O'Reilly CH, Huber M, Woollings T, Zanna L (2016) The signature of low-frequency oceanic forcing in the Atlantic multidecadal oscillation. Geophys Res Lett 43:2810–2818. https://doi.org/10.1002/2016GL067925
Pohlmann H, Smith DM, Balmaseda MA, Keenlyside NS, Masina S, Matei D et al (2013) Predictability of the mid-latitude Atlantic meridional overturning circulation in a multi-model system. Clim Dyn 41:775–785. https://doi.org/10.1007/s00382-013-1663-6
Robson JI, Sutton RT, Smith DM (2012) Initialized decadal predictions of the rapid warming of the North Atlantic Ocean in the mid 1990s. Geophys Res Lett. https://doi.org/10.1029/2012GL053370
Robson J, Polo I, Hodson DLR, Stevens DP, Shaffrey LC (2017) Decadal prediction of the North Atlantic subpolar gyre in the higem high-resolution climate model. Clim Dyn 50:921–937. https://doi.org/10.1007/s00382-017-3649-2
Scaife AA, Smith D (2018) A signal-to-noise paradox in climate science. NPJ Clim Atmos Sci. https://doi.org/10.1038/s41612-018-0038-4
Smith DM, Eade R, Scaife AA, Caron L-P, Danabasoglu G, DelSole TM et al (2019) Robust skill of decadal climate predictions. NPJ Clim Atmos Sci 2:13. https://doi.org/10.1038/s41612-019-0071-y
Tseng YH, Lin H, Chen HC, Thompson K, Bentsen M, Böning CW et al (2016) North and equatorial Pacific Ocean circulation in the core-II hindcast simulations. Ocean Model 104:143–170. https://doi.org/10.1016/j.ocemod.2016.06.003
Wang Q, Ilicak M, Gerdes R, Drange H, Aksenov Y, Bailey DA et al (2016a) An assessment of the Arctic Ocean in a suite of interannual CORE-II simulations. Part I: sea ice and solid freshwater. Ocean Model 99:110–132. https://doi.org/10.1016/j.ocemod.2015.12.008
Wang Q, Ilicak M, Gerdes R, Drange H, Aksenov Y, Bailey DA et al (2016b) An assessment of the Arctic Ocean in a suite of interannual CORE-II simulations. Part II: liquid freshwater. Ocean Model 99:86–109. https://doi.org/10.1016/j.ocemod.2015.12.009
Yashayaev I (2007) Hydrographic changes in the labrador sea, 1960–2005. Prog Oceanogr 73:242–276. https://doi.org/10.1016/j.pocean.2007.04.015
Yeager S (2015) Topographic coupling of the Atlantic overturning and gyre circulations. J Phys Oceanogr 45:1258–1284. https://doi.org/10.1175/JPO-D-14-0100.1
Yeager S, Danabasoglu G (2014) The origins of late-twentieth-century variations in the large-scale North Atlantic circulation. J Clim 27:3222–3247. https://doi.org/10.1175/JCLI-D-13-00125.1
Yeager SG, Robson JI (2017) Recent progress in understanding and predicting Atlantic decadal climate variability. Curr Clim Change Rep 3:112–127. https://doi.org/10.1007/s40641-017-0064-z
Yeager S, Karspeck A, Danabasoglu G, Tribbia J, Teng H (2012) A decadal prediction case study: late twentieth-century North Atlantic ocean heat content. J Clim 25:5173–5189. https://doi.org/10.1175/JCLI-D-11-00595.1
Yeager SG, Karspeck AR, Danabasoglu G (2015) Predicted slowdown in the rate of Atlantic Sea ice loss. Geophys Res Lett 42:10704–10713. https://doi.org/10.1002/2015GL065364
Yeager SG, Kim WM, Robson J (2016) What caused the Atlantic cold blob of 2015? US CLIVAR Var 14:24–31
Yeager SG, Danabasoglu G, Rosenbloom NA, Strand W, Bates SC, Meehl GA et al (2018) Predicting near-term changes in the earth system: a large ensemble of initialized decadal prediction simulations using the community earth system model. Bull Am Meteorol Soc 99:1867–1886. https://doi.org/10.1175/bams-d-17-0098.1
Zhang R (2010) Latitudinal dependence of Atlantic meridional overturning circulation (AMOC) variations: LATITUDINAL DEPENDENCE OF AMOC VARIATION. Geophys Res Lett. https://doi.org/10.1029/2010GL044474
Zhang R, Vallis GK (2007) The role of bottom vortex stretching on the path of the North Atlantic western boundary current and on the northern recirculation gyre. J Phys Oceanogr 37:2053–2080. https://doi.org/10.1175/jpo3102.1
Zhang R, Sutton R, Danabasoglu G, Delworth TL, Kim WM, Robson J et al (2016) Comment on "The Atlantic Multidecadal Oscillation without a role for ocean circulation". Science 352:1527–1527